COMPREHENSIVE AERODYNAMIC AND ACOUSTIC INSIGHTS INTO THE VOLOCOPTER-2X DURING FLIGHT

Moritz Muth
Research Associate

Manuel Keßler
Professor

University of Stuttgart
Stuttgart, Germany

ABSTRACT

The aerodynamic behavior and aeroacoustic signature of the Volocopter 2-X aircraft are studied by performing high-fidelity CFD simulations during climb and descent. To gain more detailed insight into the flight states, three half-model simulation setups were investigated: an isolated rotor configuration, a setup without the fuselage and a full aircraft model. Additionally, the noise emissions of these configurations were simulated using a Ffowcs Williams-Hawkings based computational aeroacoustic (CAA) code and were compared to flight test measurements. Realistic flight conditions for the simulations were achieved by performing a flight-mechanical trim of the half model and adapting the rotor speeds to achieve a periodic state for the acoustic simulations.

The VC-2X demonstrates both rotor–rotor and rotor–structure interactions that affect the aerodynamic performance and acoustic emissions. While interactions with the fuselage and supporting beams induce additional thrust fluctuations, rotor–rotor interactions remain the dominant source of unsteady aerodynamic effects. Blade–vortex interactions (BVI) were identified in both examined flight conditions, with increased intensity during descent. In contrast, the climb condition revealed stronger rotor wake–structure interactions. A comparison between the half-model simulations and flight test data shows good agreement in terms of overall sound pressure levels and spectral content. This indicates that the half-model approach is capable of predicting noise under realistic flight conditions. However, the prediction of specific tonal components and directivity patterns showed discrepancies due to additional effects such as crosswinds and rotor speed variability in flight test.

NOTATION

*

Symbols

c_l Sectional lift coefficient [-]

c_T Thrust coefficient [-]

u Flight speed [m/s]

p Pressure [Pa]

$OSPL$ Overall sound pressure level [dB]

RPM Revolution per minute [1/min]

SPL Sound pressure level [dB]

T_{std} Thrust standard deviation [N]

η Relative rotor efficiency [%]

ρ Density [kg/m³]

*

Acronyms

BPF blade passing frequency

BVI blade vortex interaction

CAA computational aeroacoustic

IDDES improved delayed-detached eddy simulation

FFT Fast Fourier Transformation

FW-H Ffowcs Williams-Hawkings

UAM urban air mobility

VC-2X Volocopter-2X aircraft

INTRODUCTION

Multirotor aircraft are becoming increasingly prominent in civil aviation, driven by advances in battery and propulsion technologies that enable new vertical take-off and landing (VTOL) concepts. As a result, multirotor propulsion systems are now being integrated into larger VTOL configurations, with a growing focus on applications involving human transportation. This development is paving the way for a new field of application: Urban Air Mobility (UAM), for which the first successful demonstration flights have already been conducted (Refs. 1, 2). Conventional VTOL designs face limitations in urban surroundings due to stringent environmental and noise regulations. Encouraging the development of electric-powered configurations such as multicopters, tiltrotors or distributed propulsion systems. Most of these concepts are characterized by at least two, usually multiple rotors in compact configurations like Volocopter's VoloCity with 18 rotors or the Joby S4 with 6 tilting propellers.

Compared to conventional helicopters, these designs exhibit fundamentally different aerodynamic and acoustic behaviors with unique signatures. Key differences include the use of smaller rotors, reduced tip Mach numbers, and additional aerodynamic interactions with the required installation structures. The rotors, operating at low induced velocities, are prone to interact with their self-generated tip vortices, contributing to blade-vortex interaction (BVI) in multirotor aircraft. This phenomenon is amplified due to the increased number of rotors compared to a traditional helicopter designs. However, the smaller rotor size typically results in a weaker tip vortex, resulting in less intense individual BVI events. Despite this trend, the overall acoustic impact can be significant due to the cumulative effects of the high number of rotors and their complex airframe integration. As a result, rotor–rotor and rotor–structure interactions produce both broadband and tonal noise components. These installation effects, typical of multicopter and drone configurations, can significantly alter the perceived noise with additional broadband contributions and high-frequency tonal elements. Consequently, noise reduction is critical for UAM aircraft certification and public acceptance. Surveys and psychoacoustic studies show that people are concerned about the noise emission of eVTOLs and may find them more annoying than regular road vehicles despite similar sound levels (Refs. 3, 4).

Accurate prediction and reduction of aircraft noise is therefore of great interest. Previous studies have focused on the individual effects occurring on eVTOLs, such as small-scale rotor acoustics, rotor-rotor and rotor-structure interactions. A significant amount of research was conducted analyzing rotors and their parameters in hover or forward flight (Ref. 5). Celik et al. (Ref. 6) carried out experimental studies to understand the aeroacoustic characteristics of UAM rotors in tandem configurations. They investigated the influence of rotor spacing, free-stream velocities, and tilt angles on the performance of the rotors. Their findings showed that the presence of an upstream rotor and the rotor-rotor spacing have a significant influence on the emitted noise characteristics and the first blade passing frequency (BPF). In addition, the rotor tilt angle also affects these parameters, while increasing the free-stream velocity causes an increase in the broadband noise emission. Since eVTOLs are equipped with a higher number of rotors compared to conventional helicopters, additional support structures are required to mount them to the fuselage. These structures introduce further rotor-structure interactions. Muth et al. (Ref. 7) performed aerodynamic and acoustic simulations of a section of the Volocopter-2X's support structure with one and three rotors in hover. Their results showed that installation effects lead to increased thrust fluctuations, although the mean thrust remains comparable to that of an isolated rotor. These fluctuations generate additional noise emission at higher harmonics and change the noise directivity. Nevertheless, in the three-rotor configuration studied, rotor-rotor interactions had a more significant influence than installation effects.

However, the noise emission also strongly depends on the flight state. Takeoff and landing are expected to play a major role due to prolonged exposure times, higher blade loading, altered inflow conditions, and proximity to the surroundings. Chaudhary et al. (Ref. 8) studied the approach and departure noise of a hexacopter through flight tests and simulations. They observed a higher noise level during descent compared to climb maneuvers. Additionally, an increase in forward flight velocity resulted in lower noise emissions. Vertical velocity variations showed opposing trends for climb and descent, higher descent rates leading to increased noise emissions.

In recent years, increasing computational capabilities have sparked growing interest in the simulation of complete eVTOL concepts. Higgins et al. (Ref. 9) studied the aeroacoustic emissions of a tiltrotor aircraft, focusing on the associated nonlinear interactions between the multirotor configuration and the airframe. Their study covered both hover and forward flight, displaying higher noise levels during hover. The influence of rotor synchrophasing was also examined and fount to have a positive effect on the noise levels at the aircraft surface while altering the overall sound radiation pattern. Jia and Lee (Refs. 11, 12) investigated the acoustics of NASA's 1- and 6-passenger UAM concept quadcopter in forward flight. Their results indicated a dominant influence of BVIs, with additional higher harmonic noise due to root induced interactions. They found no significant effects from the fuselage and no interactions between the rotor blades, due to the large spacing between the rotors. The simulation results were also compared to a conventional Bell 430 helicopter, showing that both configurations produce significantly lower noise levels, with the 1-passenger aircraft even being completely masked by highway noise during cruise. Thai et al. (Refs. 13, 14) studied a pre-production prototype of the Joby Aviation tiltrotor aircraft in various flight states. They performed aeroacoustic simulations and compared them to flight test data, finding good agreement at low frequencies, though the relevant noise sources and flow phenomena showed deviations. Additional modeling of airframe shielding and broadband noise improved the predictions. Further a framework was developed to predict approach and departure noise using CFD-based noise hemispheres along the trajectory. While the model tended to overpredict noise, the inclusion of shielding effects, refined hemisphere resolution, and added terrain showed observable improvements. Finally, the Volocopter VC-2X has been studied by Miesner et al. (Refs. 15, 16) with respect to its aerodynamic performance in different flight states and in near-ground conditions. Their half-model approach, which was validated against full-model setups, showed only minor deviations. Additionally, Cléro et al. (Ref. 17) presented a study of an acoustic measurement campaign conducted with the VC-2X near Paris in 2022. They analyzed the ground-based sound levels under various flight conditions, including hover, cruise, approach and take-off.

This paper investigates the acoustic characteristics of the VC-2X in climb and descent flight using high-fidelity simulations and compares the results with measurements performed by Volocopter GmbH. The aim is to identify the dominant noise sources and validate the simulations with experimental results.

THE VOLOCOPTER-2X

The Volocopter 2X is the third generation multirotor aircraft developed by Volocopter GmbH in Bruchsal, Germany. Unveiled in 2017 as a first operational demonstrator, the VC-2X has since performed numerous public test flights. Featuring 18 rotors arranged over 6 interconnected rotor segments, the VC-2X showcases a unique design that provides a large total rotor disk area while enabling low noise emissions and high maneuverability. Each rotor is powered by its own electric motor, allowing precise control of rotor speeds. Unlike conventional helicopters, the VC-2X lacks both a tail rotor and cyclic or collective rotor control. Instead, orientation and flight speed are controlled by adjusting the individual rotor speeds.

NUMERICAL APPROACH

The simulation framework introduced in this section comprises of the CFD solver FLOWer, the CAA solver ACCO and the BEM Tool ScatMan. FLOWer is managed via a HPC Python-based communication interface, allowing automated CFD simulation runs. Aeroacoustic evaluation is performed as a post-processing step using the CFD data within the ACCO and ScatMan Tools.

High-Order Navier-Stokes Solver: FLOWer

For this work, the proven state-of-the-art IAG rotorcraft simulation framework was applied to multicopter applications. The block-structured, finite-volume unsteady Navier-Stokes CFD solver FLOWer was used to perform the simulations presented. Originally developed at the German Center for Aerospace (DLR) (Ref. 18), FLOWer has been continuously extended at the IAG (Ref. 19), including state-of-the-art Delayed Detached Eddy Simulation (DDES) methods (Ref. 20). Based on the method of lines, the CFD solver simulates the governing differential equation with a separate spatial and temporal discretization. Temporal discretization is achieved using an implicit second-order dual time-stepping approach combined with a three-step multigrid method to accelerate the convergence of the applied Runge-Kutta scheme (Ref. 21). Spatial discretization is performed by either a second-order central difference Jameson-Schmidt-Turkel (JST) scheme (Ref. 22) or various high-order weighted essentially nonoscillatory (WENO) schemes (Ref. 23). In this investigation, the Reynolds-Averaged Navier-Stokes (RANS) equations are closed using the Menter-SST turbulence model assuming fully turbulent flow. A Chimera grid overset technique is used to enable the simulation of rotating structures such as multicopters and to simplify mesh generation.

Computational aeroacoustics: ACCO

The computational aeroacoustics code ACCO, developed by IAG, is used to compute and propagate acoustic signals into the far field (Ref. 24). Converged CFD simulation solutions in the form of data extraction over time are used to calculate the noise emission. ACCO is based on the Ffowcs Williams–Hawkings equation

$$
\begin{aligned}
\frac{\overline{\partial}^2\overline{\rho}'}{\partial t^2} - c^2\overline{\nabla}^2\overline{\rho}' &= \frac{\partial^2}{\partial x_\mathrm{i}\partial x_\mathrm{j}}[T_\mathrm{ij}H(f_\mathrm{s})] \\
&- \frac{\partial}{\partial x_\mathrm{i}}[(p'n_\mathrm{i}) + \rho u_\mathrm{i}(u_\mathrm{n} - v_\mathrm{n}))\delta(f_\mathrm{s}) \\
&+ \frac{\partial}{\partial t}[(\rho_0 v_\mathrm{n} + \rho(u_\mathrm{n} - v_\mathrm{n}))\delta(f_\mathrm{s})\ , \quad (1)
\end{aligned}
$$

which models acoustic emissions using aerodynamic quantities such as density (ρ') and pressure (p') fluctuations. The equation includes physical terms such as the normal vector n_i, the normal component of the fluid velocity u_n , the normal component of the surface velocity v_n, the Dirac delta function δ, the Lighthill tensor T_{ij}, and the Heaviside function $H(f_s)$. Sound propagation to defined far-field observer positions is performed using Lighthill's acoustic analogy, represented by the wave operator on the left side of the Eq. 1. The FW-H approach herein uses a permeable integration surface for the computation, while the flow outside of the integration volume is assumed to be an undisturbed freestream. This surface can either coincide with the physical surface of the body, capturing its associated pressure fluctuations, or be an external integration surface that encloses all relevant flow structures, especially those resulting from interaction effects. The right-hand side of Eq. 1 represents the acoustic source terms generating the sound waves and accounts for monopole (volume displacement), dipole (unsteady surface loading), and quadrupole (turbulence and compressibility) contributions.

The presented simulation framework has been widely applied in aerodynamic and aeroacoustic analyses of rotorcraft designs. In recent years, the framework has also proven effective for high-fidelity simulations of novel eVTOL and multicopter configurations. For instance, a detailed CFD and aeroacoustic investigation of a complete H145 helicopter in descent flight was conducted by Kowarsch (Ref. 25). Besides conventional helicopter designs, the FLOWer solver has demonstrated its capabilities to simulate the aerodynamic and acoustic behavior of multirotor systems, such as distributed propulsion systems (Ref. 26) and tandem rotor configurations (Ref. 27). The coupled CFD-CAA approach was recently validated in an investigation of a fixed-pitch UAV rotor under varying flight conditions by comparison with low- and mid-fidelity codes and experimental data (Ref. 28).

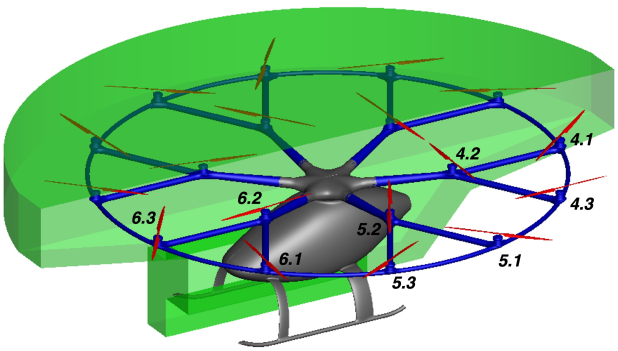

Figure 1: Overview of the VC-2X CFD model. Highlighted in blue and red are the additional simulation setups considered. The green surface represents a surrounding permeable integration surface used in the CAA evaluation.

SIMULATION SETUP

CFD Setup

To accurately capture the aerodynamic and acoustic characteristics of the VC-2X, the complete aircraft geometry, including the motor covers, fuselage, and skids, is considered in the simulation setups. The 18 rotors are arranged in two concentric circles with radii of 2.1 and 4.1 rotor radii, respectively, on the support structure. This structure is referred to as the rod structure and consists of six interconnected segments. For simplicity, the rotor blade attachments are omitted. Furthermore, the investigated rotor blade is developed by Volocopter and the transition area between the two blades of a rotor is realized by a closed elliptical section for the simulations. Overall, this setup should provide a highly accurate representation of the flow field around the VC-2X. Due to the high computational cost of full-model acoustic simulations and the geometric symmetry of the VC-2X along its central axis, a half model with suitable symmetric boundary conditions is employed. The setup is illustrated in Fig. 1. To determine the influence of rotor-rotor and rotor-structure interactions, additional simulations of isolated rotors and configurations without the fuselage are performed. These configurations are color-coded in Fig. 1.
Table 1 displays the grid block and cell amount used for this study. To resolve acoustic phenomena, each rotor blade was

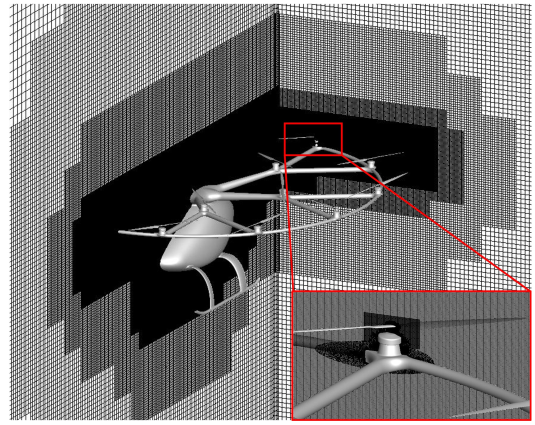

Figure 2: Simulation model of the VC-2X with off-body refinement mesh and a close-up of the rotor hub region.

resolved with $160\times112\times52$ cells in the chordwise, spanwise and normal directions. This results in approximately one million cells per blade. To account for tip, leading and trailing edge effects, the surface mesh was refined in these regions to a resolution of lower than 1‰ of the chord length. For the entire blade $y^{+} < 1$ is ensured to sufficiently resolve the boundary layer, while the structural elements are resolved accordingly. In order to obtain the most accurate representation of the aeroacoustics, all surfaces are resolved to capture frequencies up to the 50^{th} BPF with at least 20 points per wavelength. All body meshes are extruded normal to the geometry surface up to cells 10% the size of the blade chord. The only exception is the blade hub region. Here an extrusion of only 5% chord is used to avoid mesh overlap and to better represent the flow field in this area. All geometries are embedded in a Cartesian off-body (OB) mesh using the chimera technique. The OB mesh was created using hanging grid nodes to reduce computational cost. To meet the same quality criteria as the blade meshes, the finest domain of the OB mesh is set to 10% of the chord length with a refinement to 5% at the hub positions. To account for possible interaction effects near the airframe, the finest OB area is further extended around the VC-2X. In total, the OB mesh has an extension of over 175 rotor radii in each direction to prevent interference from the boundaries, while the investigated configurations are placed according to their position in the full model configuration. The CFD model placed in the OB mesh and the refinement of the hub region is visualized in Fig. 2. This setup ensures wave propagation of the pressure disturbances without excessive numerical dissipation. At the same time, an extraction of explicit flow perturbations from the finest domain of the OB mesh can be used as a CAA integration surface.

This study covers two distinct flight conditions - take-off and approach - that reflect key parts of a typical flight profile, as described in the flight-test section. The simulations are set up to replicate the environment conditions of the measurements. All simulations are initially computed using a second-order JST scheme to accelerate convergence and suppress start-up effects. Subsequently, a fifth order WENO scheme is applied to resolve flow phenomena and vortex structures along with interaction effects as accurately as possible. A flight-mechanic trim is conducted after initial convergence to determine the individual rotor RPMs and the pitch angle. Each trim cycle consists of five reference rotor revolutions to ensure full convection along the geometry. The trim is stopped after achieving residuals less than 0.1 m/s^2 translational acceleration and 0.1 rad/s^2 rotational acceleration. To enable periodic acoustic evaluation, the trimmed RPMs must be adjusted to provide periodicity, thus the RPMs are grouped and averaged to maintain deviations of less than 5%. The IDDES version of the Menter-Shear Stress Transport (SST) turbulence model was used to solve the RANS equations. It was verified that the boundary layer flows were treated in the RANS mode, while the LES mode used the maximum cell length in each index direction as the filter width. For all simulations, the flow was modeled as fully turbulent. To accelerate CFD convergence, a time step of 1.0° azimuth is applied and later reduced to 0.25° azimuth during the output phase to ensure sufficient resolution of acoustic signatures. For CAA post-processing with *ACCO*, a database with at least one full revolution of the flow field assumed to be periodic or a fully time-resolved CFD simulation is mandatory. In this study, 12 revolutions are used for acoustic evaluation, preceded by four revolutions to ensure periodicity and blending.

CAA Setup

The data used for the CAA evaluation is extracted from the CFD solution at each time step. Since the primary noise drivers in the considered cases are lift and load fluctuations caused by the rotors, the integration surface for the FW-H equation is chosen to coincide with the physical surface solution. In addition, a permeable integration surface is placed around the entire aircraft to capture interaction effects in the flow field. This surface is shown in green in Fig. 1.
The pressure signature is extracted for each time step, resulting in a sampling frequency of 28800 Hz. For the acoustic evaluation, the time domain acoustic pressure was computed at different receiver positions (called observers) in the far field. Three individually placed observers are

Table 1: Overview of the grid components of the Volocopter 2X CFD setup (half model).

Component	N_{Blocks} [-]	N_{Cells} [10^6]
Background	32468	265.5
Fuselage	84	0.803
Hub structure	116	0.890
Rod structure	1563	15.74
Skid system	286	2.288
Motor cover	9×30	9×0.283
Rotor blade	18×90	18×0.992
Total	36407	305.6

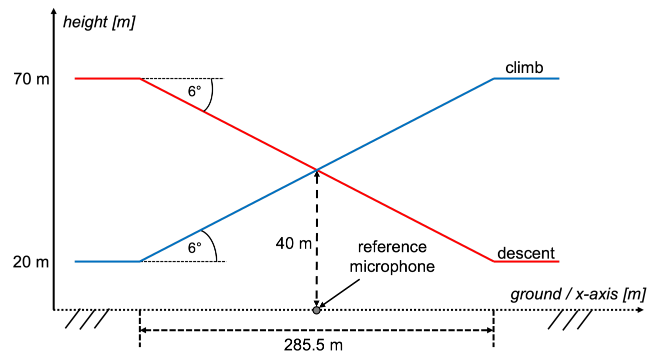

Figure 3: Targeted flight paths for the descent (red) and climb (blue) measurements.

used corresponding to the center and the most outer two microphones from the flight tests (see Fig. 3). In addition, the directivity of the noise emission is investigated using a sphere of observers surrounding the setups. To achieve this, a radius of 50 m and a resolution of 7.50° in azimuth and 3.75° in elevation are used. The sphere is centered at the center of gravity of the full VC-2X aircraft to compare the results between the different flight states. Further post-processing of the time domain pressure history is achieved by performing a Fast Fourier Transformation (FFT) to obtain the sound pressure level (SPL & OASPL) at the observer positions.

Flight-Test Setup

To evaluate the aeroacoustic predictive capabilities of the simulations, flight tests with the VC-2X aircraft were conducted by Volocopter GmbH. Inspired by the helicopter noise certification rules and regulations (Ref. 29) and visualized in Fig. 3, the flight path followed a descent respectively climb angle of 6° at a flight speed of $u_{flight} = 50\,km/h$. In addition to a center microphone, which is overflown at an altitude of 40 m above ground, a total of 20 beyerdynamic MM1 microphones were positioned perpendicular to the flight track at various lateral distance up to ± 60 m. In deviation from the rules for noise certification, the microphones were mounted upside down on tripods above ground plates, with a defined spacing of 5 mm to induce total ground reflection. This setup yields an amplitude gain of + 6 dB due to the resulting reflection. The measurements took place at an airfield in Bruchsal, Germany. The microphone array was placed on a grassy field to minimize lateral ground reflections. Each microphone is connected to a measurement box that recorded the pressure time history and transmitted the data via WLAN to a central measurement PC to allow real-time tracking. Prior to a test run, microphones were calibrated using a 1000 Hz reference signal that emits defined sound wave at 94 dB SPL. The acoustic post-processing was performed according to the ICAO evaluation procedure. Additionally, the location of the VC-2X was recorded via GPS and used to reconstruct the flight trajectory and generate flight-test noise spheres for comparison with simulated directivity patterns.

RESULTS

The following two sections investigate the characteristics of the VC-2X. The first section uses simulation data to evaluate the aerodynamics, the flow field and installation effects across different flight states. The second section analyses the aircraft's aeroacoustic signatures and compares the simulation results with measurements performed by Volocopter GmbH.

Aerodynamics

Initially, the rotor loads of the full simulation setup are compared to the results of the isolated rotor configuration. The aerodynamic quantities are obtained by recording and averaging five full rotor revolutions. Table 2 illustrates the percentage differences between the rotor quantities of the investigated setups. Overall efficiency and thrust show only minor differences between the setups, with deviations less than 4%. This indicates that the dominant interactions in a rotor system consisting of multiple adjacent rotors are due to rotor-rotor interactions, which are also present in the isolated configuration. For both flight conditions, the rear rotors (rotor group 4) experience a reduction in thrust and efficiency compared to the isolated configuration, while the front rotors display an increase. This trend is more pronounced in the descent case compared to the climb flight condition. A similar trend at the rear rotors can be seen for the thrust fluctuations. The other rotors exhibit a different characteristic, which varies depending on the flight state. The climb condition tends to increased thrust fluctuations, while the descent case leads to weaker fluctuations. This behavior is mainly due to changes in the flow field, which cause vortex structures to convect out of the rotor plane in descent conditions. This is consistent with previous studies of VC-2X geometries that demonstrated rotor-rotor interactions to have a stronger influence on thrust fluctuations than rotor-structure interactions (Ref. 7).

To better identify the underlying differences due to the airframe installation, Fig. 4 and Fig. 17 (in Appendix A) illustrate the blade sectional loads. These loads are determined by integrating the blade loads along the blade chord at discrete radial sections. The result is then normalized to the respective radial segment length. Thrust differences are shown by subtracting the isolated rotor configuration results from the entire half-model. In addition, the same approach is used for the delta between the half-model setup and the setup without the fuselage to identify the influence of the fuselage on the rotor thrust. Evaluating the integral rotor metrics reveals a pronounced difference between rotor 6.2 and the other rotors. This behavior is due to the blockage of the fuselage, which significantly increases the thrust for rotor 6.2. This increase can be seen in area [1] of Fig. 4. The installation effect of the fuselage is also visible for the rear rotor group, especially for rotor 4.2. In contrast to rotor 6.2 the airframe generates a significant vortex structures buildup behind the hub and fuselage (see area [2]). This produces additional drag and reduces the efficiency as observed in Table 2.

A comparison of the flight conditions reveals that the overall impact of the hub and fuselage installation effects is very similar in both cases, despite significant differences in the inflow conditions. While the absolute values in areas [1] and [2] differ depending on the flight condition, the general trend remains unchanged. The outer rotors are mainly influenced by the support structure, which connects the individual rotors and causes local thrust increases [3]. The support structure also prevents the formation of long lasting vortex structures between the adjacent rotors, reducing the thrust fluctuations compared to the isolated configuration. Finally, the presence of the installation modifies the flow field through blockage effects, generating additional vortex structures such as rolled-up tip vortices and interactions between various vortex structures. These secondary vortices interact with the downstream rotors, inducing additional thrust fluctuations. This effect is more pronounced in the climb case, as the vortex structures are convected beneath the rotor plane, whereas in the descent case, the vortices remain more confined above the rotor plane. This leads to stronger thrust variations along a revolution ([4]) and the observed higher thrust fluctuations compared to the descent case. As shown in Fig. 17 in the appendix, the delta thrust sectional loads between the full setup and the setup without the fuselage display a similar trend of increased fluctuations for the climb case for almost all rotors. This indicates that the additional fluctuations observed are due to the installation of the fuselage.

Flow Field Characteristics To further examine the flow field and the interactions between the vortex structures and the airframe, a detailed view of the vorticity field is examined. Therefore, Fig. 5 displays the time-averaged vorticity magnitude on three different slices oriented parallel to the centerline of the fuselage. To highlight the vortex structures, an identical logarithmic color scale is selected for all plots. The VC-2X geometry is also included to be able to assign and identify occurring interaction effects. The planes are located in the forward section, along the center hub beam, and in the aft part of the fuselage to study the airframe-induced flow changes.

The location of the first plane, Figure 5a and 5b, corresponds to the flow field around the area of maximum thrust of rotor 6.2 (refer to Figure 4). The plot illustrates the installation effects and the blockage caused by the fuselage, which lead to increased thrust for rotor 6.2. The tip vortices from rotors 6.2 and 6.3 interact with each other and impinge on the front section of the fuselage. There, the vortices are blocked and redirected upwards, resulting in an increase of the local thrust at rotor 6.2. These structures are visible in the plots, having been convected above the rotor plane and the central hub of the airframe.

Comparing the climb and descent conditions reveals that the descent case exhibits more pronounced vortex structures, since the tip vortices are directly convected upward and away from the fuselage due to the flight state. In contrast, the interactions between the fuselage and the vortex structures are significantly stronger in the climb case. Here, the flight path

Table 2: Comparison of integral rotor loads between the entire VC-2X and the isolated rotor setup.

	rotors								
	rotor 4.1	rotor 4.2	rotor 4.3	rotor 5.1	rotor 5.2	rotor 5.3	rotor 6.1	rotor 6.2	rotor 6.3
					climb				
η [%]	−2.726	−0.922	2.143	1.401	3.218	−0.610	1.796	7.687	2.281
ΔC_T [%]	−1.106	0.921	0.994	1.094	2.057	−0.363	0.427	3.684	−0.932
ΔT_{std} [%]	−3.489	−16.84	14.54	8.086	−7.580	−3.322	3.596	34.77	−1.644
					descent				
η [%]	−2.076	−10.76	−1.964	−0.414	3.552	−1.264	2.262	11.874	2.595
ΔC_T [%]	−1.277	−2.611	1.194	0.011	1.046	0.128	−0.449	4.397	0.510
ΔT_{std} [%]	−17.30	−1.717	−29.13	−8.066	3.105	−10.37	−2.213	25.40	−3.304

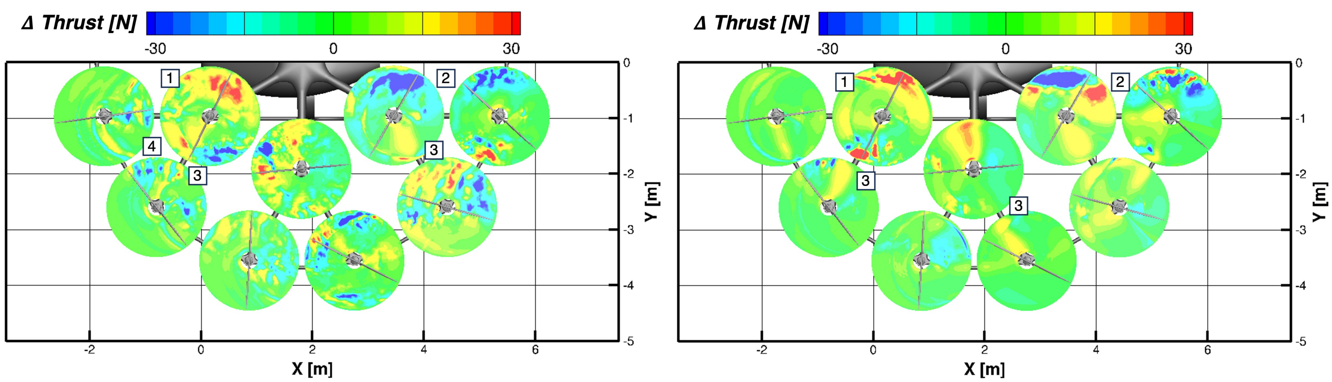

(a) Climb.

(b) Descent.

Figure 4: Delta sectional loads over the VC-2X in reference to the isolated rotor setup in various flight conditions.

leads to a downward convection of the tip vortices towards the fuselage, causing them to be redirected upwards upon contact. This interaction increases fluctuations, as evidenced by the thrust standard deviation in Table 2. Under the rotor plane secondary vortices occur in close proximity to the fuselage for the climb case. In descent, a distinct separation between the fuselage and vortices under the rotor plane are observed. These characteristics lead to increased pressure fluctuations on the airframe, which increase the induced noise emission of the structure. In contrast to this observation, the vortex structures stay in close proximity of the rotor plane or are convected above it under descent conditions. This reduces interactions of vortex structures with subsequent rotors, while the interaction with self produced vortices is increased. Both flight conditions additionally show a quick decomposition of wake sheets into smaller structures due to the proximity of the installation.

The second plane is aligned along the center hub beam (see Fig. 5c and 5d) and intersects the center of rotor 5.2. Both flight conditions show strongly pronounced tip vortices at the edge of the rotor disc. In climb flight, the vortex structures below the rotor plane are more intense and larger compared to the first plane, with multiple vortex cores interacting in the wake. This leads to additional interactions of secondary vortex structures with the side of the fuselage and the skids. In contrast, these characteristics are not observed in descent. This is primarily due to the fact that the tip vortices do not interact extensively in the wake but rather remain close to the rotor plane, resulting in increased blade vortex interactions (BVI) but fewer interactions with the fuselage. The center vortex structure is growing above the hub area for both flight conditions, but for the descent case these structures are transported further upwards reducing the interactions near the hub structures.

The last plane is located between rotor 5.3 and 4.2 in the aft part of the fuselage. The trends for the flow field observed in the first two sections is also visible in this plane. In climb condition, the tip vortices at the edge of the rotor plane grow stronger and show a clear roll-up. At the same time, the wake sheets of rotor 5.3 display no major interference, while the decay into secondary structures due to interactions with the beam structures is visible under the rotor hub. In contrast to the previous planes, the whole area around the fuselage is characterized by a large amount of small scale vortex structures. It should be noted that the interactions and vortex structures on the fuselage of the climb condition are primarily induced by the interactions of tip vortices and wake structures. Meanwhile, the descent case exhibits vortex structures mainly generated by flow separation. These separation-induced vortices interact with the rotors and their wakes, leading to increased thrust fluctuations and localized thrust increases of the sectional loads (see Fig. 4b and Fig. 17b)). Finally, the tip

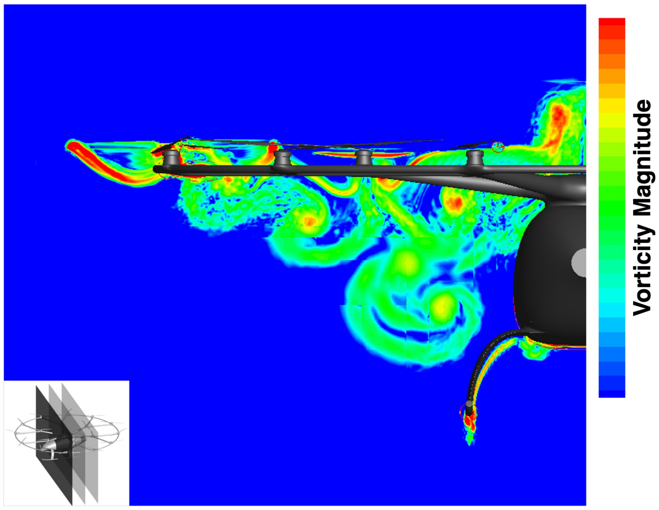

(a)

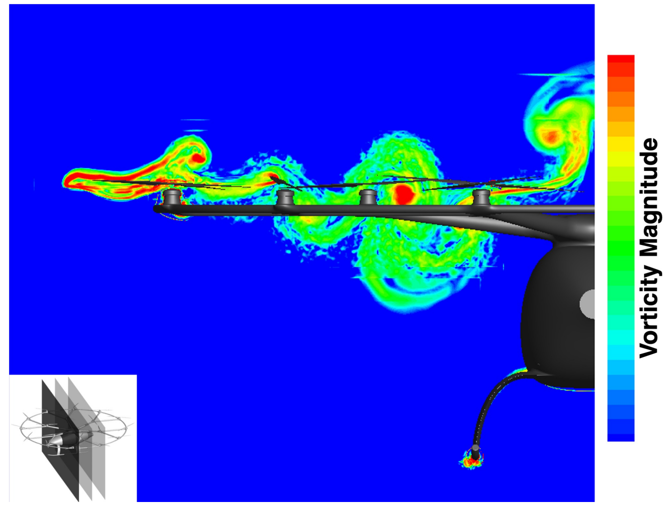

(b)

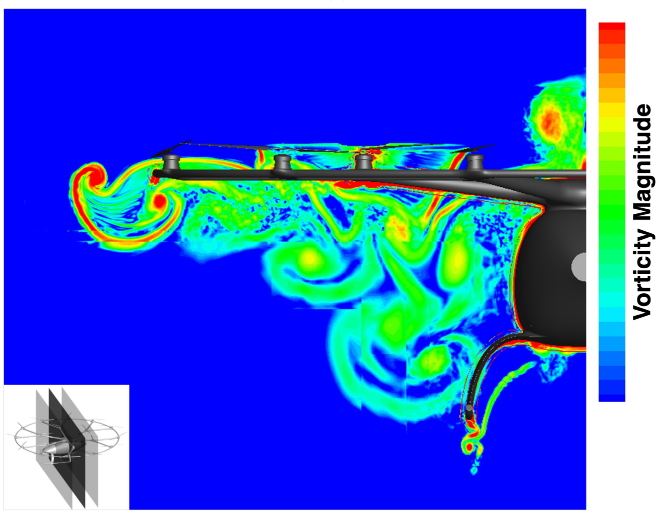

(c)

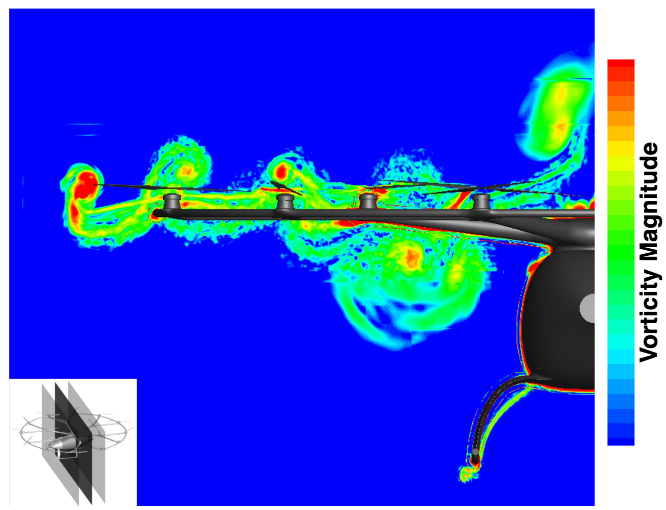

(d)

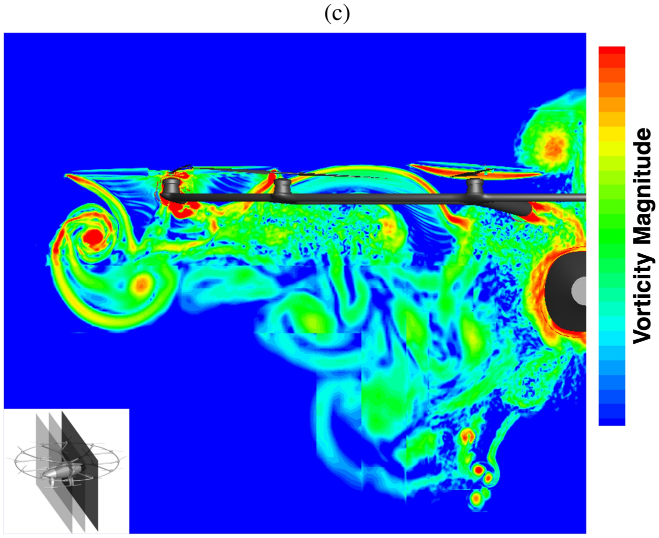

(e)

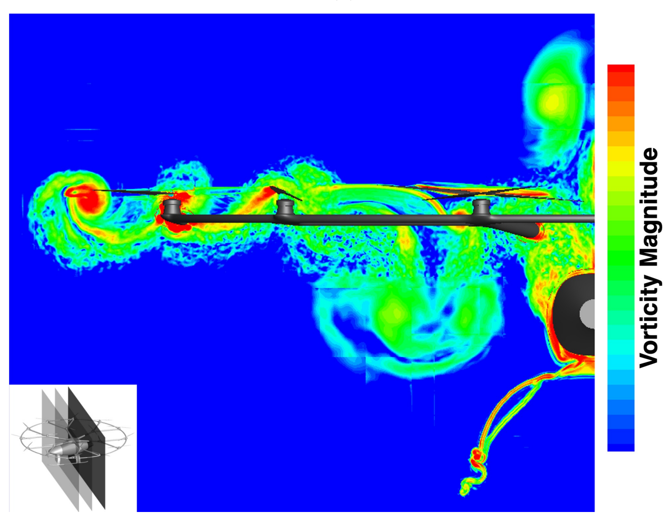

(f)

Figure 5: Visualization of flow features using time-averaged vorticity magnitude on various slices during climb (a,c,e) and descent (b,d,f).

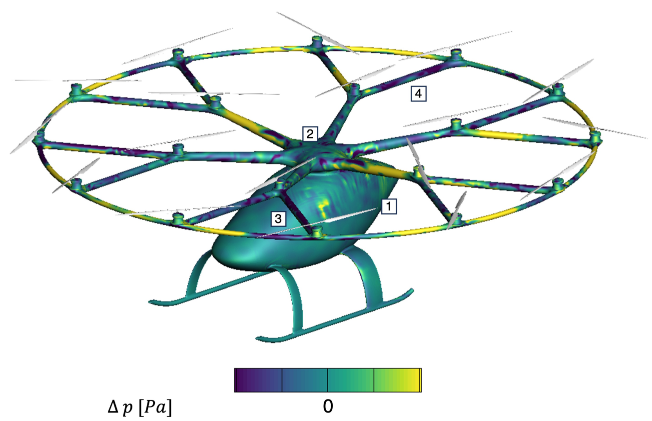

Figure 6: Instantaneous surface pressure on the VC-2X airframe in climb condition.

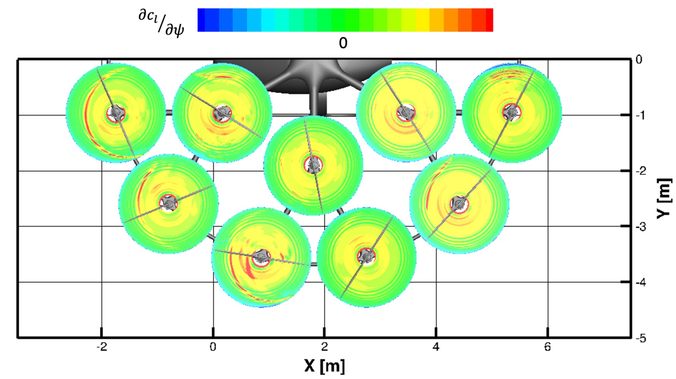

(a) Climb flight state.

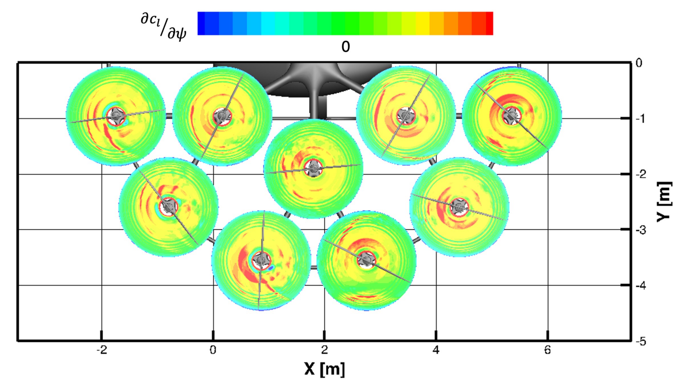

(b) Descent flight state.

Figure 7: Azimuthal derivative of the sectional lift coefficient ($\delta c_l/\delta\Psi$) for the complete VC-2X setup in different flight conditions.

vortices of the outer rotors display an increased strength due to the roll-up of these structures, which remain directly in the rotor plane and cause BVI, as discussed in detail later.

The interactions between the rotors and the fuselage do not only affect the rotor loads and the flow field, but also the surface pressure on the supporting structure. The flight condition, potential field and produced vortex structures of the rotors create pressure fluctuations on the installation, primarily the beams, hub and fuselage. These fluctuations are visualized in Fig. 6 for the climb flight state. At the back half of the fuselage (1) the tip vortices impinge the fuselage, causing distinct pressure fluctuations. This alternating pattern is disturbed by the decay of vortex structures behind rotor 5.2 (see Fig. 5e). On top of the VC-2X geometry (2) stronger pressure fluctuations with a more random characteristic are observed. These interactions are primarily due to the build-up of large vortex structures above the hub region and their interaction with the installation. Overall the strongest fluctuations occur on the beam structure of the VC-2X (3 & 4). The downwash of the individual rotors dominates the pressure fluctuations on the beams, with higher-frequency fluctuations occurring near the regions of closest rotor proximity. In these areas, rotor–rotor interactions generate vortex structures that cause additional unsteady loading, resulting in higher frequent fluctuations. Further toward the aft section of the VC-2X (4), stronger pressure fluctuations on the beams are observed, which are induced by vortex structures originating from upstream rotor–structure interactions.

BVI Investigation For conventional helicopters, unsteady loading noise during descent flight, caused by BVI, has been widely studied (Ref. 25). The flow field of the investigated VC-2X already shows indications of possible interactions between the rotors and tip vortices. The following section examines these interactions in detail and compares the influence of different flight conditions. Since one of the primary drivers for aeroacoustic impulsive noise emission is the rate of load change on the blades, the azimuthal derivative of the blade load is used to identify these effects. In Fig. 7, the azimuthal derivative of the sectional lift coefficient c_l, averaged over 5 rotor revolutions, is shown in polar coordinates for both flight states. The climb case shows significant local load fluctuations at the front outer rotors (6.1 and 6.3). These interactions are primarily due to the interactions of the subsequent rotor blade with tip vortices transported towards the inner rotor plane. These effects become even stronger for rotor 5.3, where the upstream tip vortex and the self-induced tip vortex interact, creating large rolled-up vortex structures. Near the fuselage, smaller high frequent fluctuations are observed caused by the previous mentioned fuselage interactions. Notably, the aft rotors do not experience short strong load fluctuations, as the disturbed inflow and the overall flow field rapidly convect tip vortices out of the rotor plane. This reduces BVI but increases vortex-structure interactions. In contrast, the descent simulation results show pronounced azimuthal load fluctuations for all rotors, as illustrated in Fig. 7b. The observed BVI-driven load fluctuations, particularly at the front rotors, have a higher frequency than those observed during climb. The interactions at the middle outer rotors (5.3 and 5.1) have also clearly increased. Further, the results show a local BVI event at the outside of rotor 5.1, which corresponds with the observed vortex structures in Fig. 5e. The inner and aft rotors, in particular, exhibit strong load gradients near the hub areas. These interactions are primarily caused by vortex structures generated through the interaction with the beam structure, leading to significant non-rotor-induced load fluctuations. This is evident from the way the effects depend on the installation angle of the rotors, with interactions occurring at locations of closest proximity between rotors and surrounding installation. In these areas, the generation of high-frequency, non-rotor-harmonic noise is expected. Overall, the results indicate a strong influence of BVI depending on the flight states. This suggests that the noise spectrum of the descent case will be stronger affected by higher-harmonic noise than in the climb case.

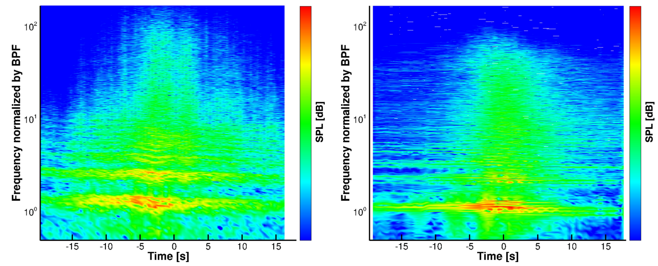

(a) Flight data.

(b) Simulation.

Figure 8: Spectral analysis of climb flight noise at center microphone.

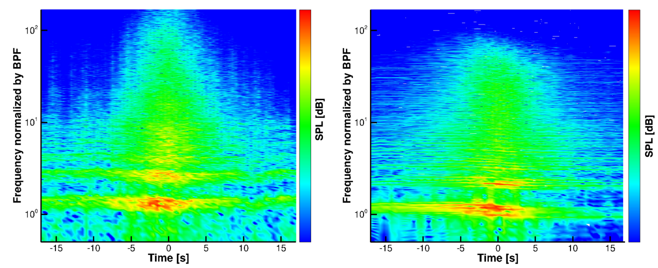

(a) Flight data.

(b) Simulation.

Figure 9: Spectral analysis of descent flight noise at center microphone.

Acoustic evaluation

After studying the aerodynamic effects, the acoustic performance is investigated in the following section. The acoustic pressure at the observer positions is calculated using the CAA solver ACCO. The acoustic results are based on the CFD data for an interval of twelve rotations, with four additional rotations used to blend the data and reduce possible transient effects at the beginning and end of the pressure history (Ref. 19). For the flyover simulations, the data is repeated up to 70 times and spatially shifted according to the current aircraft position to accurately capture the flyover characteristics. To identify the influence of the support structure, the different CFD setups are evaluated individually as integration surfaces. For validation, the simulation results are compared with test data recorded by Volocopter GmbH. The simulations are matched to the environmental conditions of the flight tests, except wind conditions. The pressure time histories from the flight tests are processed separately for each microphone. The data is divided into narrow frequency bands of $\Delta T = 0.5\,\text{s}$, and an aeroacoustic evaluation is performed for each band. Simultaneously, GPS data is used to reconstruct the flight path and assign the relative aircraft position to the timestamps of the narrowband data. All flight test data sets were arranged according to the flyover time. These data sets were then used to reconstruct noise spheres. A single sphere for every flight condition was achieved by combining data from multiple flyovers through interpolation and averaging. The flight tests were conducted at an outdoor airfield, which introduced background noise into the pressure time histories. A background noise filter, analogous to (Ref. 30), was tested but showed only negligible effects on the results. Consequently, the unfiltered data is presented in this study. Finally, all flight test data from corresponding test conditions were averaged, with standard deviation error bars added to indicate the variability of the individual tests.

Comparison to Flight Tests The different flight conditions are compared using spectral analysis. Figure 8 shows the spectrogram of a fly-over recorded at the center microphone, whereas Fig. 9 illustrates the corresponding results for the descent condition within the same time frame. For visualization purposes, the results are referenced to a baseline BPF corresponding to the lowest RPM in the simulation setup. Overall, the trends for both flight test data sets are quite similar (see Fig. 8a & 9a). Noise emission during flyover time is primarily dominated by the first BPF, though higher harmonics, especially the second BPF, also contribute to the noise characteristics. The descent condition exhibits a stronger noise emission of higher harmonics than the climb case. This acoustic signature corresponds to the the observed higher BVI for this particular flight case, as previously mentioned. In contrast, the climb case displays increased noise emission before and after the flyover. The noise signature of the climb is spread over a wider frequency range compared to the descent data, which is more concentrated around the BPF and its harmonics. This characteristic becomes more pronounced after the flyover and may be induced by the observed interactions with the fuselage. Additionally, the climb case exhibits a distinct Doppler effect due to the aircraft's movement relative to the microphone. No similar behavior is found for the descent case, indicating that the necessary RPM changes to stabilize the aircraft are larger than the expected Doppler shift. This is also evident from the wider frequency range around the first BPF, showing the highest sound pressure levels.
The flight test data is in good agreement with the simulation results shown in Fig. 8b & 9b. Similar overall characteristics including higher BVI in descent and distinct BPF harmonic noise signatures at $\pm 10\,\text{s}$ can be seen in the simulations. In contrast to the flight test data the BPF signals of the simulations are more pronounced to individual frequencies. This

is because the RPMs are fixed in the simulations and do not match the RPM variations observed in the flight test. Furthermore, both simulation spectrograms show higher noise emissions before the flyover time. This is primarily due to the fact that the RPMs of the nine rotors are fixed to three predefined values, as some periodicity is needed to reduce the required CFD input data. This leads to constructive interference effects at specific frequencies, resulting in the observed higher noise emissions. Additionally, previous studies have shown that the employed IDDES simulations slightly overestimate the noise produced at the first harmonic, enhancing the noise emissions (Ref. 7). Finally, it should be noted that this characteristic is not present after the flyover, as discussed later in the noise directivity evaluation.

Fly-over Noise After comparing the spectral characteristics of the flight test data and the simulation results, the predictive capability of the numerical tool chain is further evaluated by comparing the overall sound pressure levels at different microphone positions.

$$\begin{aligned} f_{min} &= \frac{min|RPM| \cdot n_{blades}}{60} \cdot (1 - \frac{u}{c}) \\ f_{max} &= \frac{max|RPM| \cdot n_{blades}}{60} \cdot (1 + \frac{u}{c}) \end{aligned} \quad (2)$$

Although the IDDES simulations performed include the dominant aeroacoustic noise sources, the current numerical setup does not represent mechanical, high-frequency broadband, or background noise. Therefore, the presented acoustic signals are further evaluated after being filtered according to their BPF. A conventional BPF filter is unsuitable for these flight conditions, since the Doppler effect cannot be neglected as illustrated in Fig. 8 & 9, and due to the already mentioned RPM variations in the flight tests. Therefore, the minimum and maximum frequencies for the filtering are determined as described in Eq. 2. Since the flight tests exhibit the largest RPM variations, the minimum frequency is set based on the lowest RPM observed for the respective flight state, while the maximum frequency is defined vice-versa. For the computation the flight speed of the aircraft (u) is considered. To obtain the OSPL from the filtered signal, all spectral contributions within the defined range are summed up. Thus, the resulting OSPL values represent only the noise emitted around the first BPF, excluding contributions from other frequencies, such as background or mechanical noise.

Figure 10 displays both the total OSPL (blue) and the frequency-filtered OSPL histories (red) at the center and outermost microphones for the climb condition. For comparison, the flight test data is included with the error bars indicating the standard deviation between the individual flyovers. The plots reveal good agreement between the simulations and measurements of the total OSPL histories. For both microphone positions, the simulation OSPL values before and during the aircraft's passage over the microphone array match the measurements well, both qualitatively and quantitatively. Note that the

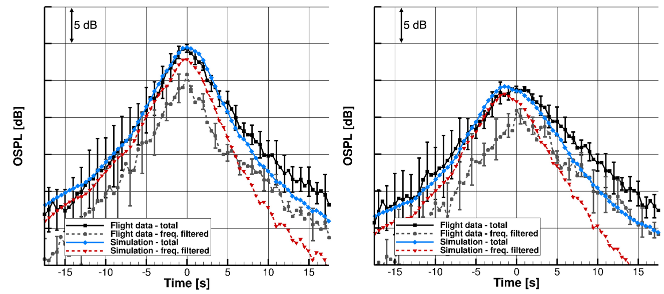

(a) Center microphone. (b) Outer microphone.

Figure 10: Comparison of the overall climb flight noise (OSPL) time history of different microphone positions.

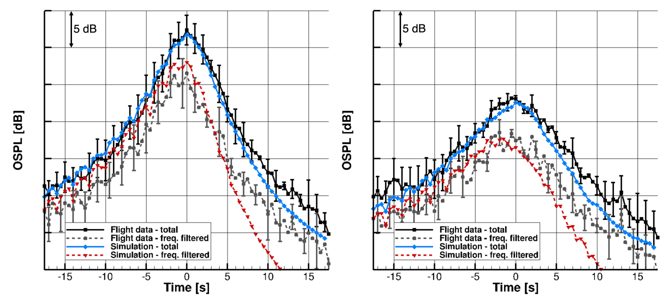

(a) Center microphone. (b) Outer microphone.

Figure 11: Comparison of the overall descent flight noise (OSPL) time history of different microphone positions.

larger error bars, especially in the time range -15 $< t <$ -10, are due to the VC-2X's low noise emission at larger distances and background noise interference. After the aircraft passes, the simulation results underestimate the measurements. This trend intensifies for the outer microphone. The causes of these observations will be investigated in the next section. In contrast to these findings, the frequency-filtered OSPL history shows a distinct overestimation of 2–4 dB in the simulations compared to the flight test data. However, the overall trends match the measurements at the center microphone. These results, in combination with the spectrograms, indicate that the flight test data is notably influenced by higher-frequency components, whereas the simulations are mainly dominated by the first BPF range. Additionally, this overestimation can be attributed to constructive interference effects caused by the fixed RPM settings in the simulations, as previously described. For the outer microphone an offset between the peak OSPL values of the both frequency-filtered results is evident.

Figure 11 illustrates the same analysis for the descent case. Overall, the results closely resemble those made for the climb condition. It should be noted that the simulation OSPL values still slightly overestimate the measurements in the frequency-filtered evaluation, though the deviations are significantly smaller at both microphones. This can be attributed to the more pronounced BVI and the stronger overall influence of rotor noise emissions in the descent case compared to the climb. Furthermore, the peak shift observed at the outer microphone during climb is not present in the descent case, resulting in a

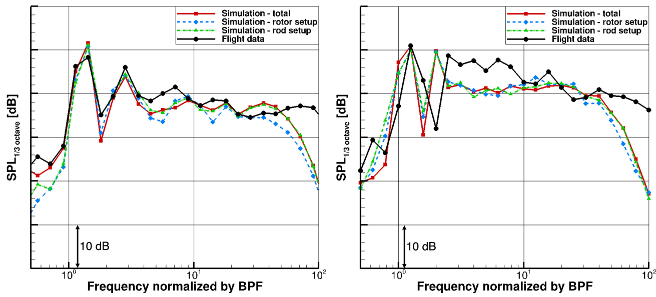

(a) Climb flight condition. (b) Descent flight condition.

Figure 12: Comparison of one-third octave band FFT results for different flight states at fly-over time.

good agreement with the measured flight test data.
The tonal components are further analyzed using FFT spectra at the time of flyover, motivated by the previously observed overestimation in the frequency-filtered OSPL results. Figure 12 presents these spectra for both climb and descent conditions, alongside results from different simulation configurations. Due to the RPM variability in the flight test data, a direct spectral comparison is not practical. Therefore, the results are presented using one-third octave bands. The results show distinct signatures of the simulations compared to the flight test data. For the climb case the data is in good agreement over the investigated BPF range for all simulation setups. The overestimation of the OSPL observed in the frequency-filtered results primarily results from the overprediction of rotor thrust and the use of higher rotor speeds than in the flight tests. Furthermore, only minor differences are observed between the various simulation configurations for the first ten BPFs. Slightly elevated SPL values are seen in the full configuration, which includes fuselage and beam structures, indicating added rotor–structure interactions and thrust fluctuations. At higher frequencies, these interactions lead to increased noise emissions. This is primarily due to the beam structures, as simulations without the fuselage produce nearly identical results to those of the complete VC-2X configuration. This behavior is not observed in the descent case shown in Fig. 12b. The descent case shows similar noise emissions for all simulation setups for harmonics greater than the second BPF, suggesting that rotor-induced noise, particularly due to BVI, is the primary contributor to the overall acoustic emission in this flight condition. Additionally, the BVI measurements display clearly higher values than the simulations in this frequency range, resulting mostly from broadband noise and vortex interactions, which are not fully resolved in the simulations.

Noise Directivity The noise directivity of the different flight conditions is analyzed to compare the overall characteristics and the influence of the installation and flight states. Therefore, the measurement signals of all 21 microphones of the test campaign were used to reconstruct a noise hemisphere around the VC-2X. The results are evaluated against the data from the mirrored full configuration simulation. Figure 13 illustrates the climb case results, and Fig. 14 shows the descent flight state. During the flight tests, both flight cases displayed similar noise emissions in relation to overall trends and absolute values. The maximum noise emission was recorded in front of the aircraft, with lower noise emissions in the rotor plane and behind the VC-2X. The descent case, in particular, exhibits an asymmetrical noise pattern, with higher values on the right side of the fuselage (positive y-axis). These asymmetric trends are due to roll and yaw angles, as well as side winds during the flight tests. Because the VC-2X orientation is controlled by the rotor RPMs, variations in the aircraft's orientation lead to higher thrust and noise emissions on one side of the aircraft. However, such effects cannot be reproduced in the simulations, since the half-model approach neglects all roll and yaw effects. This results in the observed symmetrical noise emissions. These match the overall characteristics of the flight test data. As previously discussed, the maximum noise emission is slightly overestimated by 1-2 dB. Additionally, the simulation results imply higher noise emissions underneath the aircraft. For the descent case, this high noise emission area is also present diagonally behind the fuselage. An overestimation underneath the VC-2X can be caused by neglecting shading and scattering effects at the fuselage. Further studies will include a BEM code to evaluate the scattering and shading effects of the fuselage. Besides this observation, the descent case exhibits a more confined region of peak sound pressure levels compared to the climb case. This trend is evident in both the simulations and the measurements. The frequency-filtered directivity plots further confirm these findings, as shown in Appendix B.

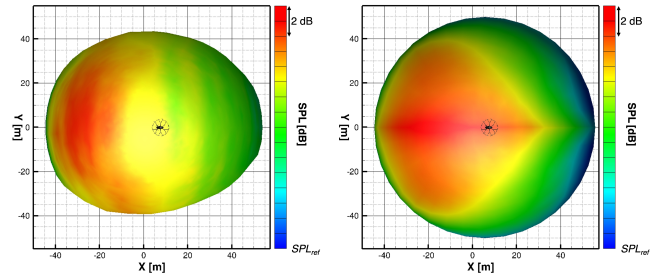

(a) Flight data. (b) Simulation.

Figure 13: Noise directivity comparison in climb flight.

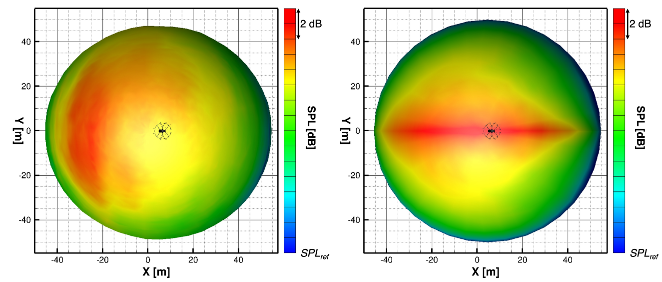

(a) Flight data. (b) Simulation.

Figure 14: Noise directivity comparison in descent flight.

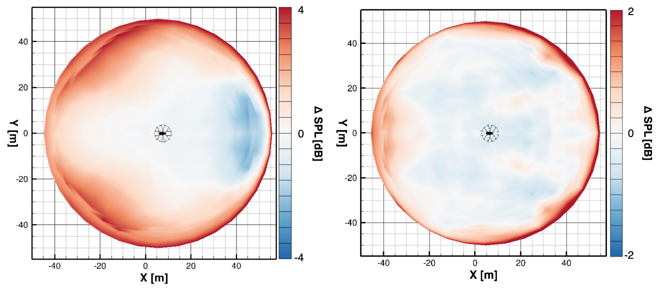

(a) Climb.

(b) Descent.

Figure 15: Delta sound pressure level between the full setup and the isolated rotor configuration simulations in different flight condition.

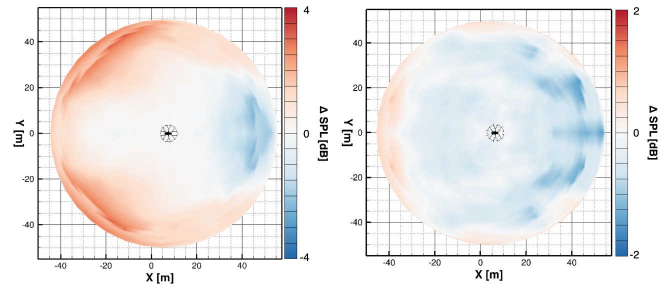

(a) Climb.

(b) Descent.

Figure 16: Delta sound pressure level of the noise directivity plots for the setup without fuselage in different flight conditions condition.

Influence of Installation Effects The influence of the installation structure, especially the fuselage, is evaluated for the simulation data in the following. Therefore, the noise hemisphere of the isolated rotor configuration is subtracted from the full-configuration setup. The results are illustrated in Fig. 15. Additionally, the delta noise plots of the setup without the fuselage to the full-configuration setup is presented in Fig. 16. The influence of the installation on directional noise emission is evident through increased SPL values near the rotor plane. While such emissions are observed in both flight states, they are more pronounced in the climb condition, with increases of up to 5 dB. This aligns with the identified interactions between rotor wakes and the fuselage, which contribute to additional noise generation. Moreover, the climb case reveals a region of reduced noise emission diagonally behind the VC-2X. This low-SPL area also appears in the comparison with the configuration without the fuselage, indicating that the reduction of up to 2.5 dB is caused by the blockage of rotors due to the fuselage installation, leading to modified rotor noise characteristics. In contrast, the descent case shows only minor deviations between different simulation setups, with differences typically staying below 2 dB. The noise increases near the rotor plane remain present but are limited to a smaller region. In comparison with the results of Fig. 16 it can be seen, that the increased noise emission in the rotor plane is primarily caused by the beam structure. The installation of the fuselage shows a similar influence on the noise emission beneath the VC-2X as observed in the climb case. The blockage of the flow field results in a reduction of rotor-rotor interactions reducing the noise emission compared to the isolated configuration. The larger deviations between the full setup and the setup without a fuselage in the area underneath the aircraft are primarily caused by additional interactions in the hub region, which influence the performance of the aft rotors.

CONCLUSIONS

This research studied the aerodynamic and aeroacoustic characteristics of the Volocopter 2-X (VC-2X) in climb and descent flight using high-fidelity CFD simulations coupled to a CAA solver. To identify individual interaction effects three half-model simulation setups were considered: an isolated rotor configuration, a configuration without the fuselage but with the beam structure, and the entire VC-2X half-model. This approach limits the simulation to zero roll and yaw angles. The aerodynamic investigation focused on the modified flow field, the affected sectional rotor loads, and the resulting fluctuations of aerodynamic quantities caused by different flight conditions and installation effects. For the acoustic evaluation, two different observer positions and a hemisphere at 50 m from the center of gravity of the VC-2X were used. The acoustic results were compared to flight test measurements performed by Volocopter GmbH. A noise hemisphere was reconstructed from the measured signals, enabling the comparison of directivity effects. All simulations were performed with the CFD solver FLOWer using a 5th order WENO scheme and the Menter-SST turbulence model in an improved DDES formulation. The solution of the CFD flow field was passed to the CAA solver ACCO to investigate the far-field noise emission. The flight states were achieved by performing a flight-mechanic trim, which was loosely coupled to FLOWer. The determined rotor RPMs were slightly modified to achieve a periodic state for the CAA computation.

1. The flow field and interactions around the VC-2X are significantly impacted by rotor-rotor interactions. Installation effects have a local impact on sectional loads and thrust fluctuations, particularly due to the redirection and accumulation of large vortex structures. Compared to the isolated rotors in both flight cases, overall thrust fluctuations are mostly reduced by installation effects, while rotor thrust and efficiency are partially increased.

2. The climb case exhibits stronger fuselage interactions compared to the descent case. The installation also induces more small-scale vortex structures to pass through the rotor plane, resulting in additional interactions compared to isolated configurations. The fuselage blockage leads to the formation of a larger vortex structure, which interacts with both the fuselage and the aft rotors, causing notable surface pressure fluctuations.

3. The descent flight case shows blade-vortex interactions for most rotors, which are distinctly stronger than in

the climb case. These interactions are further affected by blockage and redirection of the flow field and vortex structures near the beam structures. The rotors are most influenced close to the beam structures and behind the fuselage.

4. The half-model approach demonstrates good agreement with the flight test data in predicting OSPL values for both investigated flight conditions. Additionally, the spectral analysis in the form of spectrograms shows a reasonable match with the measurements.

5. The simulations tend to overestimate the produced rotor thrust and noise emission at the first BPF. Meanwhile, additional noise due to interaction, motor, and broadband noise is found at higher harmonics and frequencies, leading to underestimations in this frequency range.

6. The observed BVI noise during descent resulted in distinct emissions at higher harmonics compared to the climb case. While the simulation results captured these trends, they underestimated the measured sound pressure levels.

7. The half-model approach effectively captures the main features of directional noise emission patterns. The maximum noise emission is found to be diagonally in front of the VC-2X for both flight cases. The climb case exhibits a broader region of high SPL values in front of the VC-2X, whereas the simulations for the descent condition show maximum noise emission near the longitudinal axis. These trends contribute to increased deviations in the comparison with flight test data.

8. The flight test data exhibits distinct asymmetric directional noise patterns due to cross winds and orientation changes of the aircraft. Additional yaw and roll angles can not be replicated with the half-model setup and therefore the effects of variable rotor RPMs in respect to the longitudinal axis.

9. The installation effects on the VC-2X lead to increased noise emissions at higher harmonics (above 5 BPF) in the climb case. In contrast, due to the stronger rotor noise emissions from BVI in the descent case, these trends are less pronounced. For both flight states, slightly increased SPL values (1–3 dB) are observed at the first BPFs, attributed to the additional thrust induced by installation effects.

10. The influence of the VC-2X installation on the overall noise directivity has been demonstrated. The climb case exhibited a strong influence of the fuselage compared to the isolated rotor configuration, while the descent condition showed stronger effects due to the beam structure. The noise emission was partially reduced due to the blockage and disruption of the flow field, reducing rotor-rotor interactions.

Author contact: Moritz Muth: moritz.muth@iag.uni-stuttgart.de, Manuel Keßler: kessler@iag.uni-stuttgart.de

APPENDIX

A: Sectional loads changes between full setup and setup without fuselage

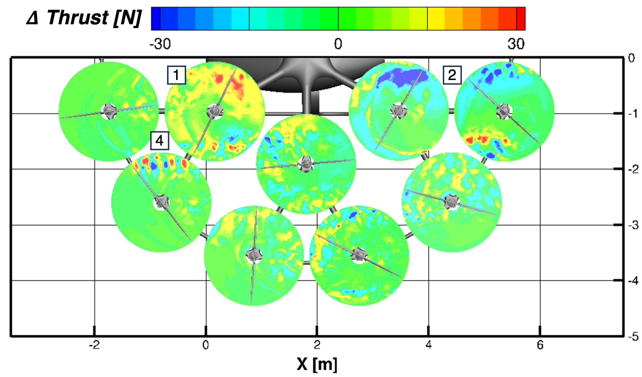

(a) Climb.

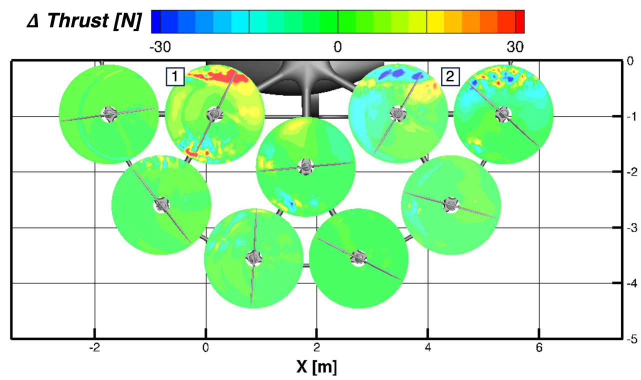

(b) Descent.

Figure 17: Delta sectional loads over the VC-2X in reference to the setup without fuselage in various flight conditions.

B: Frequency-filtered noise directivity

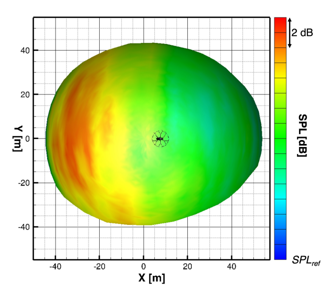

(a) Flight data.

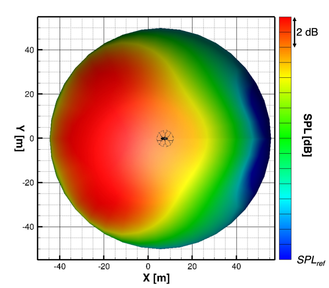

(b) Simulation.

Figure 18: Frequency-filtered noise directivity comparison in climb flight.

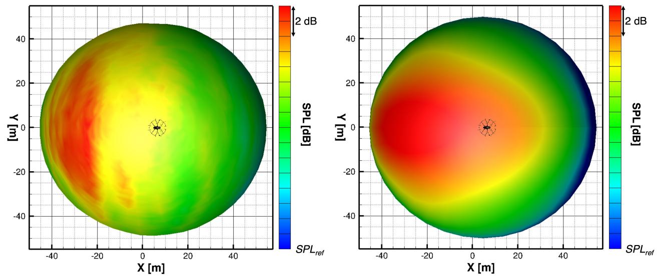

(a) Flight data. (b) Simulation.

Figure 19: Frequency-filtered noise directivity comparison in descent flight.

ACKNOWLEDGMENTS

This investigation is carried out as part of the VOLARE project. The project is a cooperation between the Institute of Aerodynamics and Gas Dynamics of the University of Stuttgart and the Volocopter GmbH from Bruchsal and has received funding from the Federal Ministry for Economic Affairs and Technology (BMWi) under grant agreement No. 20Q1954B.

The authors gratefully acknowledge Volocopter GmbH for providing configuration data and measurements, the German Aerospace Center (DLR) for access to the FLOWer code, and the High Performance Computing Center Stuttgart (HLRS) for computational resources and support on the Hawk cluster.

REFERENCES

1. Pantazis, D. N., Moussas, V., Daverona, A. C., and Argyrakis, P., "The Aerial Transport in Urban Areas: Towards the Era of Manned VTOL-AV," Computational Science and Its Applications – ICCSA 2024, Springer Nature Switzerland, 2024, pp. 422-433. isbn: 978-3-031-64605-8.

2. Kiesewetter, L., Shakib, K. H., Singh, P., Rahman , M., Khandelwal, B., Kumar, S., and Shah, K., "A holistic review of the current state of research on aircraft design concepts and consideration for advanced air mobility applications," *Progress in Aerospace Sciences*, Vol. 142, 2023, pp. 100949. DOI: https://doi.org/10.1016/j.paerosci.2023.100949.

3. Babetto, L., König, R., Fassnacht, J., and Stumpf, E., "Study on Public Acceptance of eVTOL: Safety & Noise," Deutscher Luft- und Raumfahrtkongress, Stuttgart, Germany, 2023. DOI: https://doi.org/10.25967/610319.

4. Christian, A. and Cabell, R., "Initial Investigation into the Psychoacoustic Properties of Small Unmanned Aerial System Noise," AIAA/CEAS Aeroacoustic Conference, Denver, Colorado, USA, June 2017. DOI: 10.2514/6.2017-4051.

5. Henricks, Q., Wang, Z. and Zhuang, M., "Small-Scale Rotor Design Variables and Their Effects on Aerodynamic and Aeroacoustic Performance of a Hovering Rotor," *Journal of Fluids Engineering*, Vol. 142, (8), 2020, pp. 081209. DOI: 10.1115/1.4046872

6. Çelik, A., Jamaluddin, N. S., Baskaran, K., Rezgui, D., and Azarpeyvand, M., "Aeroacoustic Performance of Rotors in Tandem Configuration," AIAA Aviation 2021 Forum, Virtual, August 2-6, 2021. DOI: 10.2514/6.2021-2282.

7. Muth, M., Keßler, K., and Krämer, E., "Aerodynamic and Aeroacoustic Investigation of Installation Effects of the Volocopter-2X Rod Structure," VFS 80th Annual Forum and Technology Display, Montreal, Canada, May 7-9, 2024. DOI: 10.4050/F-0080-2024-1098.

8. Chaudhary, R., T. Valente, V., Mukherjee, B., Jue, A., Brentner, K., and Greenwood, E., "Understanding Takeoff and Landing Noise for Small Multirotor Vehicles," VFS 80th Annual Forum and Technology Display, Montreal, Canada, May 7-9, 2024. DOI: 10.4050/F-0080-2024-1157

9. Higgins, R. J., Barakos, G. N., Shahpar, S., and Tristanto, I., "A computational fluid dynamic acoustic investigation of a tiltwing eVTOL concept aircraft," *Aerospace Science and Technology*, Vol. 111, 2021, pp. 106571. DOI: https://doi.org/10.1016/j.ast.2021.106571.

10. Zhang, T., Barakos, G. N., Filippone, A., and Furqan, "High-fidelity aero-acoustic evaluations of a heavy-lift eVTOL in hover," *Journal of Sound and Vibration*, Vol. 584, 2024, pp. 118453. DOI: https://doi.org/10.1016/j.jsv.2024.118453.

11. Jia, Z., and Lee, S., "Acoustic Analysis of a Quadrotor eVTOL Design via High-Fidelity Simulations," 25th AIAA/CEAS Aeroacoustics Conference, Delft, The Netherlands, May 20-23, 2019. DOI: 10.2514/6.2019-2631.

12. Jia, Z., and Lee, S., "Acoustic Analysis of Urban Mobility Quadrotor Aircraft," Aeromechanics Advanced Vertical Flight Technical Meeting, San Jose, California, January 21-23, 2020.

13. Thai, A., Bain, J., Mikic, G., and Stoll, A., "Flyover Noise Computations of the Joby Aviation Aircraft," VFS 79th Annual Forum and Technology Display, West Palm Beach, Florida, USA, May 16-18, 2023. DOI: 10.4050/F-0079-2023-17959.

14. Thai, A., and Bain, J., "Modeling Approach and Depature Noise of the Joby Aviation Aircraft," VFS 80th Annual Forum and Technology Display, Montreal, Canada, May 7-9, 2024. DOI: https://doi.org/10.4050/F-0080-2024-0044.

15. Miesner, S., Keßler, M., Krämer, E., and Schäferlein, U., "High-fidelity Simulation of the Volocopter-2X in cruise flight," VFS 77th Annual Forum and Technology Display, Virtual, May 10-14, 2021. DOI: 10.4050/F-0077-2021-16724.

16. Miesner, S., Keßler, M., Krämer, E., and Schäferlein, U., "Investigation of Near Ground Effects in Hover Flight for the Multi-Rotor Aircraft Volocopter 2X," VFS 76th Annual Forum and Technology Display, Virtual, October 6-8, 2020. DOI: 10.4050/F-0076-2020-16409.

17. Clero, F., Mortain, F., Le Nabat, J., Weber, D., Cabannes, T., and Sineau, M., "Acoustic Measurement of Manned Electrical Vertical Take-Off and Landing (e-VTOL) Aircraft," 30th AIAA/CEAS Aeroacoustics Conference, Rom, Italy, 2024. DOI: 10.2514/6.2024-3229.

18. Kroll, N., Rossow, C. C., Becker, K., and Thiele, F., "MEGAFLOW - a numerical flow simulation system," 21st ICAS congress, Melbourne, Australia, Sep. 1998.

19. Keßler, M., Frey, F., Letzgus, J., Öhrle, C., Thiemeier, J., and Krämer, E., "Progress in IAG's Rotorcraft Simulation Framework," *High Performance Computing in Science and Engineering '20*, Springer International Publishing, 2021, pp. 331-341. DOI: https://doi.org/10.1007/978-3-030-80602-6_21.

20. Letzgus, J., Keßler, M., and Krämer, E., "Simulation of Dynamic Stall on an Elastic Rotor in High-Speed Turn Flight," *Journal of the American Helicopter Society*, Vol. 65, (2), April 2020, pp. 1-12 (12). DOI: 10.4050/JAHS.65.022002.

21. Jameson, A., "Time Dependent Calculations Using Multigrid, with Applications to Unsteady Flows Past Airfoils and Wings," AIAA 10th Computational Fluid Dynamics Conference, Honolulu, Hawaii, June 1991. DOI: 10.2514/6.1991-1596.

22. Jameson, A., Schmidt, W., and Turkel, E., "Numerical Solution of the Euler Equations by Finite Volume Methods Using Runge Kutta Time Stepping Schemes," 14$_{th}$ Fluid and Plasma Dynamics Conference, Palo Alto, California, June 1981. DOI: 10.2514/6.1981-1259.

23. Borges, R., Carmona, M., Costa, B., and Don, W. S., "An Improved Weighted Essentially Non-Oscillatory Scheme for Hyperbolic Conservation Laws," *Journal of Computational Physics*, Vol. 227, (6), March 2008, pp. 3191– 3211. DOI: 10.1016/j.jcp.2008.11.038.

24. Keßler, M., and Wagner, S., "Source-Time Dominant Aeroacoustics," *Computers & Fluids*, Vol. 33, (5), 2004, pp.791-800. DOI: https://doi.org/10.1016/j.compfluid.2003.06.012.

25. Kowarsch, U., Öhrle, C., Keßler, M., and Krämer, E., "Aeroacoustic Simulation of a Complete H145 Helicopter in Descent Flights," *Journal of AHS*, Vol. 61, (4), October 2016, pp.1-13. DOI: 10.4050/JAHS.61.042001.

26. Wickersheim, R., Keßler, M., Sembowski, J., Bongen, D., and Gomes, J., "Numerical Investigation and Validation of Noise Sources of a Distributed Propulsion System," *AIAA Journal*, Vol. 63, (4), April 2025, pp.1418-1430. DOI: 10.2514/1.J064531.

27. Muth, M., Keßler, M., and Krämer, E., "High Fidelity Aerodynamic and Aeroacoustic Simulations of Multicopter Rotors with Anhedral During Hover and Forward Flight," VFS 79th Annual Forum and Technology Display, West Palm Beach, Florida, USA, May 16-18, 2023. DOI: 10.4050/F-0079-2023-17948.

28. Yin, J., De Gregorio, F., Rossignol, K. S., Rottmann, L., Ceglia, G., Reboul, G., Barakos, G., Qiao, G., Muth, M., Kessler, M., Visingardi, A., Barbarino, M., Petrosino, F., Zanotti, A., Oberti, N., Savino, A., Bernardini, G., Poggi, C., Abergo, L., Caccia, F., Guardone, A., Testa, C., and Zaghi, S., "Acoustic and aerodynamic evaluation of DLR small-scale rotor configurations within GARTEUR AG26," *CEAS Aeronautical Journal*, November 2024. DOI: https://doi.org/10.1007/s13272-024-00790-2.

29. International Civil Aviation Organization, *Environmental Technical Manual—Volume I: Procedures for the Noise Certification of Aircraft,* edition Doc. 9501, 2012.

30. Wickersheim, R., Keßler, M., and Krämer, E., "Fly-Over Noise Measurements of a Distributed Propulsion Flight Demonstrator," Deutsche Gesellschaft für Luft- und Raumfahrt - Lilienthal-Oberth e.V, 2024. DOI: https://doi.org/10.25967/63014.

CLASSIFICATION & COPYRIGHT